Progress In Electromagnetics Research, PIER 103, 323–338, 2010

POLAR FORMAT ALGORITHM FOR SPOTLIGHT BISTATIC SAR WITH ARBITRARY GEOMETRY CONFIGURATION

J. P. Sun and S. Y. Mao

School of Electronic and Information Engineering
Beihang University
Beijing, China

G. H. Wang

School of Electrical and Electronic Engineering
Nanyang Technological University
Singapore

W. Hong

National Key Lab of MW Imaging Technology
Institute of Electronics
CAS, Beijing, China

Abstract—This paper presents an effective Polar Format Algorithm (PFA) for spotlight bistatic synthetic aperture radar (SAR) with arbitrary geometry configuration. Nonuniform interpolation and resampling are adopted when converting raw data from polar coordinates to Cartesian coordinates according to the characteristics of raw data samples in spatial frequency space. Thus, the proposed algorithm avoids both rotation transformation and the calculation of azimuth compensation factor and thereby avoids the corresponding approximate error appeared in the conventional PFA. Meanwhile, the proposed algorithm inherits the character of decomposing 2-D interpolation to two 1-D interpolations from conventional PFA algorithm applied in monostatic SAR imaging. Therefore, the processing flow, computation efficiency and performance of the proposed algorithm are the same as those of conventional PFA for monostatic spotlight SAR. Point target simulations are provided to validate the proposed algorithm.

Corresponding author: G. H. Wang (wang0330@ntu.edu.sg).

1. INTRODUCTION

Bistatic synthetic aperture radar (SAR) obtains more flexible imaging geometry configuration than conventional monostatic SAR because of spatial separation of transmitter and receiver. Bistatic geometry can possibly contribute to various SAR functions such as passive imaging and reconnaissance, forward-looking imaging, interferometric imaging, moving target indication, etc. [1–4]. So far, some research institutes have carried out experiments [5–9]. The imaging algorithm for bistatic SAR is still in its infancy and is different from the algorithms for monostatic SAR.

There are various imaging algorithms proposed for bistatic SAR in the recent literatures. Time-domain back-projection (BP) algorithm is the most popular one in current practical application because it is applicable to arbitrary geometry configuration [4, 5, 10]. However, BP algorithm is still inefficient in computation, although fast algorithms are developed for its application in some special imaging configurations. Loffeld et al. presents an approximate formula in 2D frequency domain for the echoes of bistatic SAR with arbitrary geometry configuration. Based on the approximate formula, Omega-K algorithm [12] and 2D Inverse Scaled Fast Fourier Transform (ISFFT) algorithm [13] are proposed under different approximate conditions. In [14, 15], other two Omega-K algorithms are proposed, respectively. Besides the algorithms mentioned above, there are other bistatic SAR imaging algorithms, for example, Equivalent Monostatic Imaging algorithm [16, 17], which introduces data domain transformation, Nonlinear Chirp Scaling algorithm [18], Series Expansion algorithm [19], "NuSAR" method [20], etc.. Most of the abovementioned algorithms are developed for bistatic SAR imaging geometry with translational invariant and fixed receiver configuration.

The Polar Format Algorithm (PFA) is one of the earliest imaging algorithms adopted for spotlight SAR and is extensively applied in practical monostatic SAR systems [21, 22]. Rigling et al. for the first time proposes PFA for bistatic SAR imaging. Its main contribution is the introduction of rotation transformation and azimuth compensation factor [23]. The first result of real bistatic SAR data processed by conventional PFA is presented in [8]. It illustrates the effectiveness of conventional monostatic PFA for bistatic SAR imaging. In this paper, a new effective PFA imaging algorithm is proposed for spotlight bistatic SAR with arbitrary geometry configuration. Differing from the method proposed in [8, 23], this algorithm adopts nonuniform interpolation [24] when converting raw data from polar coordinates to Cartesian coordinates according to the characteristics of raw data

samples in spatial frequency space. Nonuniform interpolation in the proposed method also differentiates itself from that in [24] in the following ways. First, for BiSAR with arbitrary geometry configuration in this paper, the 2D spatial frequency sampling distribution is more complicated and we develop a new model. Second, the calculation of resampling index, involving the solution of a quartic equation, is much different and we propose a new computation method as well as an approximate analytical solution for the calculation. This is the main contribution of this paper over our previous work. Thus, the proposed algorithm avoids both rotation transformation and the calculation of azimuth compensation factor and thereby avoids the corresponding approximate error. Meanwhile, the trait of conventional PFA is reserved that 2-D interpolation is broken down into two 1-D interpolations. Thus, the processing flow, efficiency and performance of the new algorithm are kept approximately the same as those of conventional PFA for monostatic spotlight SAR.

2. SIGNAL MODEL OF SPOTLIGHT MODE BISTATIC SAR WITH ARBITRARY GEOMETRY CONFIGURATION

The imaging geometry of spotlight mode bistatic SAR with arbitrary geometry configuration is defined in Fig. 1. Transmitter $\mathbf{S}_T$ and receiver $\mathbf{S}_R$ are carried on moving platforms with velocities of v_T and v_R, and altitudes of h_T and h_R, respectively. The radar line of

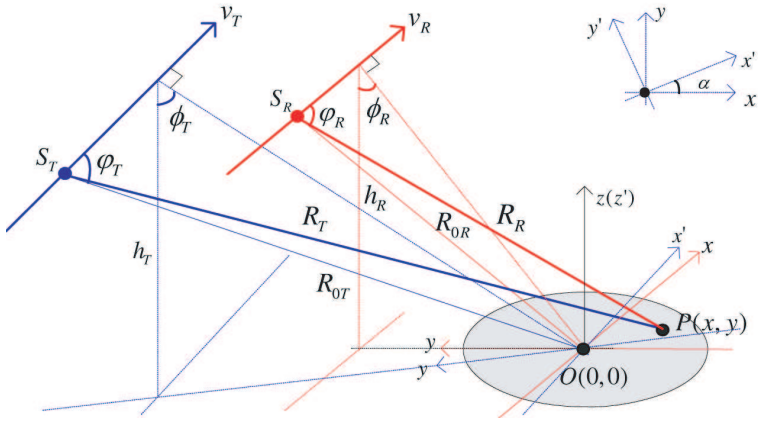

Figure 1. Imaging geometry for spotlight mode bistatic SAR of arbitrary geometry configuration.

sight (LOS) continuously points to the imaging area center O during synthetic aperture time T_a. The off-nadir angle with respect to the position of closest approach in the flight path is ϕ_T for transmitter and ϕ_R for receiver. Let t be the azimuth time. Let the instant squint angle be $\varphi_T(t)$ for transmitter and $\varphi_R(t)$ for receiver, the instant slant range between the area center O and antenna phase center be $R_{0T}(t)$ for transmitter and $R_{0R}(t)$ for receiver. We define two rectangle coordinates for imaging scene, say xyz and $x'y'z'$, both with origin O, for transmitter and receiver, respectively. Note that x and x' are parallel to the flight directions of $\mathbf{S}_R$ and $\mathbf{S}_T$, respectively. For parallel flight geometry, xyz and $x'y'z'$ are the same. For non-parallel flight geometry, the $x'y'$ coordinate system is related to the xy coordinate system by a rotation angle of α, as illustrated in Fig. 1. For the point target P, the space vector is $\mathbf{r} = (x, y, 0)$ while the instant distance to $\mathbf{S}_T$ and $\mathbf{S}_R$ is $R_T(t)$ and $R_R(t)$, respectively.

Suppose that $\mathbf{S}_T$ transmits Chirp pulse signals with center frequency f_c, pulse width T_P and chirp rate γ. Then, the echo from point target P on $\mathbf{S}_R$ can be written as

$$s_r(t,\tau)=\sigma_P \mathrm{rect}\left(\frac{t}{T_a}\right)\mathrm{rect}\left(\frac{\tau-(R_T(t)+R_R(t))/c}{T_p}\right) \exp\left\{j2\pi f_c\left(\tau-\frac{R_T(t)+R_R(t)}{c}\right)+j\pi\gamma\left(\tau-\frac{R_T(t)+R_R(t)}{c}\right)^2\right\}, \quad (1)$$

where τ is fast time. Let the reference signal for dechirping be [21]

$$s_{ref}(t,\tau)=\exp\left\{j2\pi f_c\left(\tau-(R_{0R}+R_{0T})/c\right)+j\pi\gamma\left(\tau-(R_{0R}+R_{0T})/c\right)^2\right\}. \quad (2)$$

Then the target signal after dechirping is

$$\begin{aligned} s_{IF}(t,\tau) &= s_r(t,\tau)s^*_{ref}(t,\tau) \\ &= \sigma_P \mathrm{rect}\left(\frac{t}{T_a}\right)\mathrm{rect}\left(\frac{\tau-(R_T(t)+R_R(t))/c}{T_P}\right)\exp\{\Phi\}, \end{aligned} \quad (3)$$

where

$$\begin{aligned} \Phi \;=\; & -\frac{2\pi\gamma}{c}\left(\frac{f_c}{\gamma}+\tau-\frac{R_{0T}+R_{0R}}{c}\right)(R_T-R_{0T}+R_R-R_{0R}) \\ & +\frac{\pi\gamma}{c^2}(R_T+R_R-R_{0T}-R_{0R})^2 \end{aligned} \quad (4)$$

The quadratic term in (4) is known as residual video phase which can be omitted or removed by preprocessing operation [21, 22]. The second

order approximation for $R_T - R_{0T}$ can be written as

$$\begin{aligned} R_T - R_{0T} &= |\mathbf{R}_T - \mathbf{r_t}| - R_{0T} \\ &\simeq -\frac{(\mathbf{R}_{0T} \cdot \mathbf{r_t})}{R_{0T}} + \frac{r_t^2}{2R_{0T}} + \frac{r_t^2(\mathbf{R}_{0T} \cdot \mathbf{r_t})}{2R_{0T}^3} - \frac{(\mathbf{R}_{0T} \cdot \mathbf{r_t})^2}{2R_{0T}^3} \\ &= -\frac{(\mathbf{R}_{0T} \cdot \mathbf{r_t})}{R_{0T}} + R_c \end{aligned} \tag{5}$$

where the range curvature component is

$$R_c = \frac{r_t^2}{2R_{0T}} + \frac{r_t^2(\mathbf{R}_{0T} \cdot \mathbf{r_t})}{2R_{0T}^3} - \frac{(\mathbf{R}_{0T} \cdot \mathbf{r_t})^2}{2R_{0T}^3},$$

which can be omitted under the assumption of plane wave front for the moderate resolution or the small size imaging scene. Similar operations can be performed on $R_R - R_{0R}$. After that, we obtain

$$R_T - R_{0T} \approx -\frac{(\mathbf{R}_{0T} \cdot \mathbf{r_t})}{R_{0T}} \tag{6a}$$

$$R_R - R_{0R} \approx -\frac{(\mathbf{R}_{0R} \cdot \mathbf{r_t})}{R_{0R}} \tag{6b}$$

Using the approximation results above, (4) can be rewritten as

$$\Phi \approx 2\pi K(\tau) \left(\hat{\mathbf{R}}_{0T} + \hat{\mathbf{R}}_{0R}\right) \cdot \mathbf{r_t} = 2\pi \left(f_x \cdot x + f_y \cdot y + f_z \cdot 0\right) \tag{7}$$

where f_x and f_y are the corresponding spatial frequencies of x and y

$$K(\tau) = \frac{\gamma}{c}\left(\frac{f_c}{\gamma} + \tau - \frac{R_{0T} + R_{0T}}{c}\right), \tag{8}$$

$\hat{\mathbf{R}}_{0R}$ and $\hat{\mathbf{R}}_{0T}$ are instantaneous direction vectors defined by

$$\hat{\mathbf{R}}_{0T} = \frac{\mathbf{R}_{0T}}{R_{0T}}, \quad \hat{\mathbf{R}}_{0R} = \frac{\mathbf{R}_{0R}}{R_{0R}} \tag{9}$$

According to the geometry shown in Fig. 1, we can obtain

$$\begin{aligned} \hat{\mathbf{R}}_{0T} =& (-\cos\varphi_T \cos\alpha - \sin\varphi_T \sin\phi_T \sin\alpha, \\ & -\cos\varphi_T \sin\alpha + \sin\varphi_T \sin\phi_T \cos\alpha,\ \sin\varphi_T \cos\phi_T) \\ \hat{\mathbf{R}}_{0R} =& (-\cos\varphi_R,\ \sin\varphi_R \sin\phi_R,\ \sin\varphi_R \cos\phi_R) \end{aligned} \tag{10}$$

where φ_T and φ_R vary with slow time t. The components of K at sample (k, n) in 3D spatial-frequency space can be written as

$$\begin{aligned} f_x(k,n) &= K(k)\Theta_x(n) \\ f_y(k,n) &= K(k)\Theta_y(n) \\ f_z(k,n) &= K(k)\Theta_z(n) \end{aligned} \tag{11}$$

where $k = 1, 2, \ldots, N_r$ and $n = 1, 2, \ldots, N_a$ indicate discrete sampling indexes of fast time and slow time, respectively, and

$$\begin{aligned}\Theta_x(n) &= -\cos\varphi_T(n)\cos\alpha - \sin\varphi_T(n)\sin\phi_T\sin\alpha - \cos\varphi_R(n)\\ \Theta_y(n) &= -\cos\varphi_T(n)\sin\alpha + \sin\varphi_T(n)\sin\phi_T\cos\alpha + \sin\varphi_R(n)\sin\phi_R\\ \Theta_z(n) &= \sin\varphi_T(n)\cos\phi_T + \sin\varphi_R(n)\cos\phi_R\end{aligned} \quad (12)$$

Now, we will investigate the distribution property of spatial-

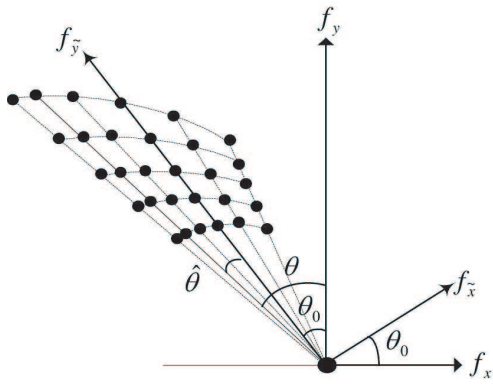

(a) initial data samples in spatial frequency space

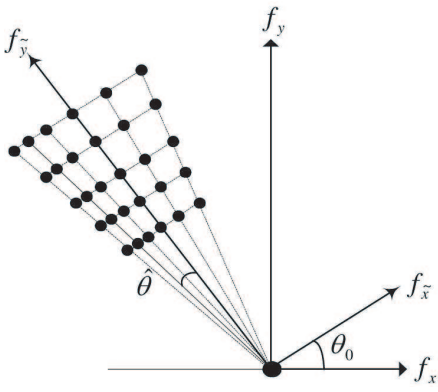

(b) samples after range interpolation

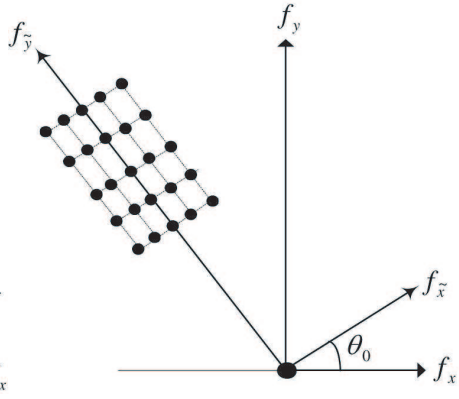

(c) samples after azimuth interpolation

Figure 2. BiSAR data samples in 2-D spatail frequency space during the overall process of polar coordinate conversion.

frequency samples in $f_x f_y$ coordinate. Assume

$$\begin{aligned} \theta(n) &= \tan^{-1}\left(-\frac{\Theta_x(n)}{\Theta_y(n)}\right), \\ \Lambda(n) &= \sqrt{\Theta_x^2(n) + \Theta_y^2(n)} \end{aligned} \tag{13}$$

and $\tilde{K}(k,n) = K(k)\Lambda(n)$. Then, we have

$$\begin{aligned} f_x(k,n) &= -\tilde{K}(k,n)\sin\theta(n) \\ f_y(k,n) &= \tilde{K}(k,n)\cos\theta(n) \end{aligned} \tag{14}$$

Thus, the distribution of spatial-frequency samples for spotlight mode bistatic SAR can be achieved through the formulas above. The typical distribution is shown in Fig. 2(a).

Since the A/D sampling frequency f_S and pulse repetition frequency (PRF) is generally fixed for certain operations, k and n are uniform space samples of fast time and slow time. From (14), it can be inferred that for the spatial-frequency samples of spotlight bistatic SAR in polar coordinate system, the distributions of polar radius $\tilde{K}(k,n)$ and polar angle $\theta(n)$, which are determined by the bistatic imaging geometry, are nonuniform. Although the sample space of $\tilde{K}(k,n)$ is uniform in time domain, the initial value $\tilde{K}(1,n)$ and the sampling interval $|\tilde{K}(k+1,n) - \tilde{K}(k,n)|$ in slant plane varies with azimuth sampling index n. Therefore, the distribution of spatial-frequency samples of spotlight bistatic SAR differs distinctively from monostatic SAR and the consequent polar-to-rectangular resampling must be different as well.

3. POLAR FORMAT ALGORITHM FOR SPOTLIGHT MODE BISTATIC SAR

The polar angle $\theta(n)$ may have a certain range according to (13). The median value θ_0 is not always zero during synthetic aperture time. When θ_0 is comparatively large, two polar interpolation methods may be applicable [21]: one is the Stabilized Scene Polar Interpolation (SSPI), the other is the Line-of-Sight Polar Interpolation (LOSPI). The advantages and disadvantages of these two methods for monostatic radar are discussed in detail in [21]. The LOSPI method is based on the rotation invariant property of Fourier Transform and is able to take full advantage of raw data samples in spatial-frequency space. However, this method requires extra computation effort because the imaging result of 2-D Inverse Fast Fourier Transform (IFFT) should be converted to xy coordinate through a coordinate

transformation. Nonetheless, it is more parctical for the ability of resolution preservation. Thus, this paper adopts LOSPI method. Typical sampling result of LOSPI is shown below in Fig. 2(c).

Let $\Delta\theta(n) = \theta(n) - (\theta(0) + \theta(N_a))/2$, the median value θ_0 can be chosen as

$$\Delta\theta(n_0) = \min_{1<n<N_a} (|\Delta\theta(n)|) \ , \ \theta_0 = \theta(n_0) \tag{15}$$

Rotate the rectangular coordinate $f_x f_y$ over an angle of θ_0 in the counter-clockwise direction and denote the resulting coordinate by $f_{\tilde{x}} f_{\tilde{y}}$, and let $\hat{\theta}(n) = \theta_0 - \theta(n)$. Then the spatial-frequency samples on $f_{\tilde{x}} f_{\tilde{y}}$ would be

$$\begin{aligned} f_{\tilde{x}}(k,n) &= \tilde{K}(k,n)\sin\hat{\theta}(n) \\ f_{\tilde{y}}(k,n) &= \tilde{K}(k,n)\cos\hat{\theta}(n) \end{aligned}, \tag{16}$$

which is shown in Fig. 2(a).

After that, interpolation process is to be performed. Similar to the PFA algorithm for monostatic SAR, the 2-D interpolation will be decomposed into two 1-D interpolations, which can be implemented by multi-phase interpolation filter [21, 22]. As what follows, we take two steps to complete the two 1-D interpolations.

In the first setp, we perform the interpolation in range direction. For interpolation in range direction, we assume the factor of up-sampling to be L_k and the sampling number be constant during interpolation and resampling. According to (16) and Fig. 2(a), for given azimuth index n the output sample index $s_k(k,n)$ with respect to range index k can be written as

$$s_k(k,n) = \text{int}\left(\frac{\tilde{K}(k,n_0)/\cos\hat{\theta}(n) - \tilde{K}(1,n)}{K(1/f_S)\Lambda(n)} L_k\right), \tag{17}$$

where Int$[x]$ represents an integer that is the round part of x. Then the spatial-frequency samples after range interpolation would be

$$\begin{aligned} f_{\tilde{x}}(k,n) &= \tilde{K}(k,n_0)\tan\hat{\theta}(n) \\ f_{\tilde{y}}(k,n) &= \tilde{K}(k,n_0) \end{aligned} \tag{18}$$

which is shown in Fig. 2(b) and indicates that a 1-D uniform interpolation is carried in the range direction.

In the second step, we perform the interpolation in azimuth direction. Before azimuth interpolation and resampling, the azimuth bandwidth after resampling should be calculated. In order to take full advantage of raw data samples, let it be

$$B_{\tilde{x}} = \left| K(1,n_0)\left(\tan\hat{\theta}(N_a) - \tan\hat{\theta}(1)\right)\right| \tag{19}$$

For interpolation in azimuth direction, we assume the up-sampling factor to be L_n and the sampling number be constant during interpolation and resampling. Then the spatial frequency sampling interval after azimuth resampling would be $\Delta f_{\tilde{x}} = B_{\tilde{x}}/N_a$, and let

$$G(k,n) = \tan\left(\theta_0 - \tan^{-1}\left(\frac{(n-n_0)\Delta f_{\tilde{x}}}{\tilde{K}(k,n_0)}\right)\right) \tag{20}$$

According to (13), the sample index $s_n(k,n)$ extracted for output with respect to azimuth index n for given range index k should satisfy the equation below

$$G(k,n) = -\frac{\Theta_x\left(s_n(k,n)/L_n\right)}{\Theta_y\left(s_n(k,n)/L_n\right)} \tag{21}$$

According to imaging geometry shown in Fig. 1, the instantaneous squint angles of platform S_T and S_R satisfy

$$\begin{aligned}\cos\varphi_R(n) &= \frac{R_{0R}(n_0)\cos\varphi_R(n_0) - v_R(n-n_0)/PRF}{R_{0R}(n)}\\ \cos\varphi_T(n) &= \frac{R_{0T}(n_0)\cos\varphi_T(n_0) - v_T(n-n_0)/PRF}{R_{0T}(n)}\end{aligned} \tag{22}$$

A quartic equation of s_n can be obtained by substituting (12), (20), (22) into (21). It is complicated to solve the equation although the analytic solution does exist. In practical, we can use numerical solution to solve it.

Let $R_{0R}(s_n/L_n)R_{0T}(n) \approx R_{0T}(s_n/L_n)R_{0R}(n)$, then the approximate analytic solution of formula (21) can be obtained as

$$s_n(k,n) \approx \text{int}\left[L_n\left(\frac{\begin{array}{l}R_{0R}(n_0)\cos\varphi_R(n_0)\\ +R_{0T}(n_0)\cos\varphi_T(n_0)\Gamma(k,n)\\ -\Pi(k,n)\end{array}}{v_R + v_T\Gamma(k,n)}PRF + n_0\right)\right] \tag{23}$$

where

$$\begin{aligned}\Gamma(k,n) =& \frac{R_{0R}(n)}{R_{0T}(n)}\left(\cos\alpha + G(k,n)\sin\alpha\right)\\ \Pi(k,n) =& R_{0R}(n_0)\left(G(k,n)\left(\sin\varphi_T(n)\sin\phi_T\cos\alpha\right.\right.\\ &\left.\left. + \sin\varphi_R(n)\sin\phi_R\right) - \sin\varphi_T(n)\sin\phi_T\sin\alpha\right)\end{aligned} \tag{24}$$

(21) and (23) indicate that a 1-D nonuniform interpolation is carried in azimuth direction. The 2-D spatial frequency samples after azimuth interpolation would be

$$\begin{aligned}f_{\tilde{x}}(k,n) &= (n-n_0)\Delta f_{\tilde{x}}\\ f_{\tilde{y}}(k,n) &= \tilde{K}(k,n_0)\end{aligned} \tag{25}$$

The output samples after interpolation process will be uniformly distributed in both azimuth and range directions as shown in Fig. 2(c). Thus, we can apply 2-D IFFT directly to get the imaging result in $\tilde{x}\tilde{y}$ coordinates. The 2-D spatial frequency sampling distribution during the overall process of polar-to-rectangular convesion for spotlight bistatic SAR is shown in Fig. 2.

According to the rotation invariant property of Fourier Transform, when the imaging result in $\tilde{x}\tilde{y}$ coordinate is required be mapped to xy coodinate, the coordinate conversion formula below can be used

$$\begin{aligned} x &= \tilde{x}\cos\theta_0 - \tilde{y}\sin\theta_0 \\ y &= \tilde{x}\sin\theta_0 + \tilde{y}\cos\theta_0 \end{aligned} \tag{26}$$

When necessary motion compensation and correction is taken into account [25, 26], a practical processing flow of the proposed PFA algorithm for spotlight bistatic SAR imaging is shown in Fig. 3. Several methods adopted in monostatic SAR are available for auto-

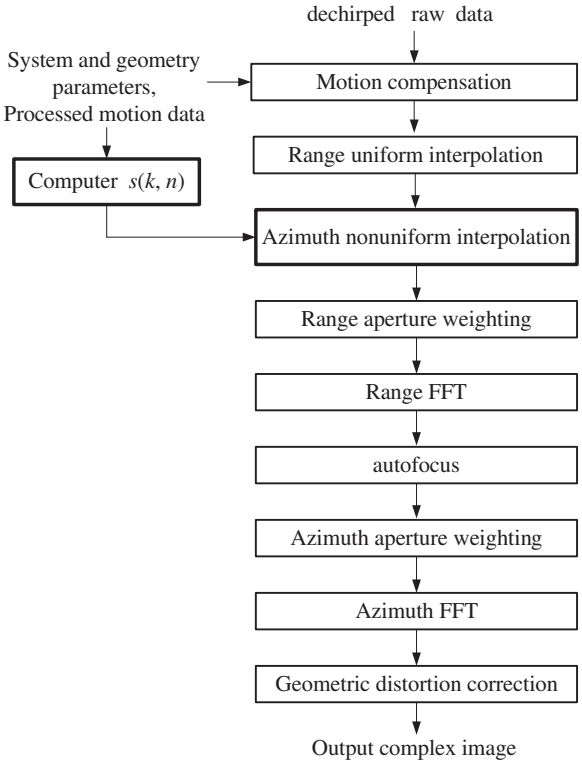

Figure 3. Processing flow of the proposed PFA for spotlight mode bistatic SAR.

focusing processing [21, 27, 28]. This processing flow is basically the same as that of PFA algorithm for squint spotlight monostatic SAR using LOSPI method. For azimuth nonuniform interpolation, extra computation in solving (21) will be needed if numerical method is applied, while the solution can be obtained before imaging. If the approximate solution in (23) is adopted, the computation efficiency and imaging performance will be exactly the same as those of monostatic PFA algorithm.

4. SIMULATION EXPERIMENT

The proposed PFA imaging algorithm is common to spotlight bistatic SARs with different geometry configurations because the imaging geometry defined in Fig. 1 is arbitraty configured. To validate the algorithm, we will show the result of a typical arbitrary imaging geometry. The radar parameters used in simulations are shown in Table 1. More practical concerns about the echo data simulation can be find in [29].

Table 1. Radar system parameters for simulation.

Parameter	Value
Center frequency	10 GHz
Chirp bandwidth	150 MHz
ADC sampling rates	100 MHz
Pulse duration	5 μs
PRF	600 Hz

Referring to the imaging geometry defined in Fig. 1, nine point targets located in ground-plane xy coordinates are shown in Fig. 4 and point P (200 m, 200 m) is chosen to analyze the performance of boundary point target response in imaging results.

Table 2. Results of point target analysis of Point P.

	azimuth	range
Resolution caculated	2.43 m	1.75 m
Resolution measured	2.49 m	1.77 m
ISLR (dB)	−8.69	−9.24
PSLR (dB)	−12.81	−13.27

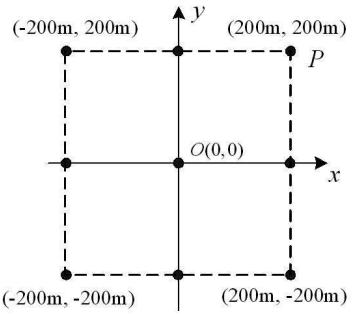

Figure 4. Location of point targets for simulation.

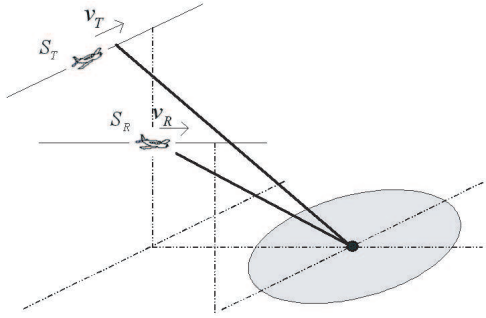

Figure 5. The BiSAR illumination geometry for simulation.

For bistatic SAR imaging with arbitrary geometry configuration, there are no limitations to platform velocity and flying path. In our simulation, the platforms are set as squint mode and the geometry configuration is shown in Fig. 5. The specific platform and geometry parameters corresponding to Fig. 1 are: $\alpha = 90°$, $v_T = 76\,\mathrm{m/s}$, $h_T = 4000\,\mathrm{m}$, $\phi_T = 60°$, $\varphi_T = 60°$; $v_R = 60\,\mathrm{m/s}$, $h_R = 3000\,\mathrm{m}$, $\phi_R = 60°$, $\varphi_R = 70°$.

Simulation results are shown in Fig. 6. Fig. 6(a) shows the imaging result in $\tilde{x}\tilde{y}$ coordinate and Fig. 6(b) indicates the output response of the chosen point target P. Results of the point target response of point P are shown in Table 2.

The ideal focusing result has PLSR $\approx -13.3\,\mathrm{dB}$, ISLR $\approx -9.8\,\mathrm{dB}$. Comparing the PFA results of this paper with the ideal ones, the IRW (Impulse Response Width) broadening is less than 5%; PLSR rising is less than 1 dB; and ISLR rising is less than 2 dB. Thus, the proposed algorithm can well meet the requirement of moderate focusing accuracy [30].

To demonstrate the computation efficiency of the proposed algorithm, we take BP algorithm as a comparison. To the best of our knowledge, BP algorithm is the only one that is suitable to the specified imaging processing in this paper. The simulations were run in a common PC with an Intel ® Core (TM2) E6550 @2.33 GHz CPU and 1 GB RAM. The size of echo data is 2048×2048. Up-sampling factor for the proposed PFA algorithm is $L_k = L_n = 6$. CPU time is 11.7 s. We take the fast BP algorithm proposed in [10] for comparison. CPU time is 135.2 s. It is obvious that our method is more efficient in computation.

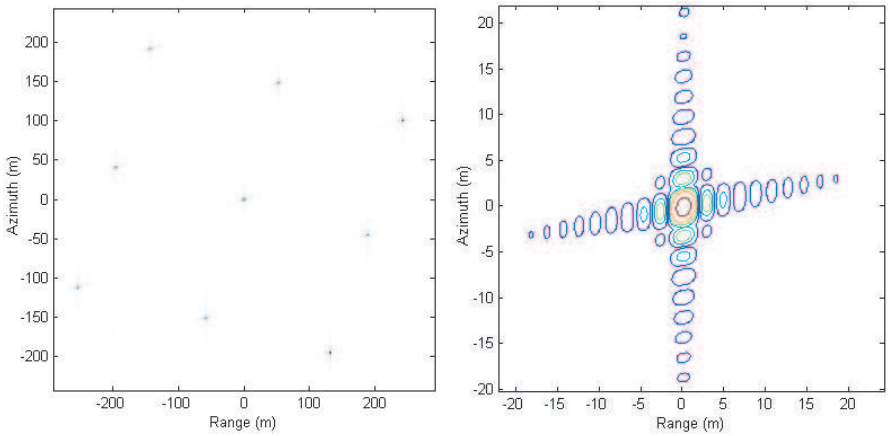

(a) BiSAR image of point targets (b) the response of point target P

Figure 6. Imaging results of proposed PFA for BiSAR.

5. CONCLUSION

This paper has proposed an effective PFA imaging algorithm for spotlight bistatic SAR working in arbitrary geometry configuration. Nonuniform interpolation and resampling are adopted in polar-to -rectangular coordinate conversion according to the characteristics of raw data samples in spatial frequency space. The proposed algorithm breaks down 2-D interpolation into two 1-D interpolations and thereby preserves the computation efficiency as conventional PFA does. Meanwhile, the sample index sequences $\{s_k(k,n)\}$ and $\{s_n(k,n)\}$ for output can be obtained before imaging process. Thus, the processing flow, computation efficiency and performance of the proposed algorithm are the same as those of conventional PFA for monostatic spotlight SAR imaging. To validate the algorithm, simulation experiments are performed for a typical arbitrary geometry configuration. Simulation studies prove that the proposed algorithm is effective in focused-imaging processing in arbitrary spotlight bistatic SAR imaging configurations of interest, such as top-view configuration and forward-looking configuration.

ACKNOWLEDGMENT

This work was supported in part by the National Nature Science Foundation of China by Grant 60901056, and the "973" Program of

China by Grant 2010CB731903. The authors would also like to thank the anonymous reviewers for improve the quality of this paper.

REFERENCES

1. BenKassem, M. J., J. Saillard, and A. Khenchaf, "BISAR mapping I. Theory and modeling," *Progress In Electromagnetics Research*, PIER 61, 39–65, 2006.
2. BenKassem, M. J., J. Saillard, and A. Khenchaf, "BISAR mapping II. Treatment, simulation and theory and experimentation," *Progress In Electromagnetics Research*, PIER 61, 67–87, 2006.
3. Krieger, G. and A. Moreira, "Spaceborne bi- and multistatic SAR: Potentials and challenges," *IEE Proc., Radar Sonar Navig.*, Vol. 153, No. 3, 184–198, 2006.
4. Ender, J., "A step to bistatic SAR processing," *Proc. of EUSAR*, 356–359, 2004.
5. Ender, J., I. Walterscheid, and A. Brenner, "New aspects of bistatic SAR: Processing and experiments," *Proc. of IGARSS*, 1758–1762, 2004.
6. Walterscheid, I., J. Ender, A. Brenner, and O. Loffeld, "Bistatic SAR processing and experiments," *IEEE Trans. Geosci. Remote Sens.*, Vol. 44, No. 10, 2710–2717, 2006.
7. Dubois-Fernandez, P., H. Cantalloube, B. Vaizan, G. Krieger, R. Horn, M. Wendler, and V. Giroux, "ONERA-DLR bistatic SAR campaign: Planning, data acquisition, and first analysis of bistatic scattering behaviour of natural and urban targets," *IEE Proc., Radar Sonar Navig.*, Vol. 153, No. 3, 214–223, 2006.
8. Yates, G., A. M. Horne, A. P. Blake, R. Middleton, and D. B. Andre, "Bistatic SAR image formation," *IEE Proc. Radar Sonar Navig.*, Vol. 153, No. 3, 208–213, 2006.
9. Marcos, J., P. Dekker, J. Mallorqui, A. Aguasca, and P. Prats, "SABRINA: A SAR bistatic receiver for interferometric application," *IEEE Trans. Geosci. Remote Sens. Lett.*, Vol. 4, No. 2, 307–311, 2007.
10. Ding, Y. and D. C. Munson, Jr., "A fast back-projection algorithm for bistatic SAR imaging," *IEEE International Conference on Image Processing*, Vol. 2, 449–452, 2002.
11. Loffeld, O., H. Nies, V. Peters, and S. Knedlik, "Models and useful relations for bistatic SAR," *IEEE Trans. Geosci. Remote Sens.*, Vol. 42, No. 10, 2031–2038, 2004.
12. Walterscheid, I., J. Ender, A. Brenner, and O. Loffeld, "Bistatic

SAR processing using an omega-k type algorithm," *Proc. of IGARSS*, Vol. 2, 10640–1067, 2005.

13. Natroshvili, K., O. Loffeld, H. Nies, A. M. Ortiz, and S. Knedlik, "Focusing of general bistatic SAR configuration data With 2-D inverse scaled FFT," *IEEE Trans. Geosci. Remote Sens.*, Vol. 44, No. 10, 2718–2727, 2006.
14. Giroux, C., H. Cantalloube, and F. Daout, "An Omega-K algorithm for SAR bistatic systems," *Proc. of IGARSS*, Vol. 2, 1060–1063, 2005.
15. Qiu, X., D. Hu, and C. Ding, "An Omega-K algorithm with phase error compensation for bistatic SAR of a translational invariant case," *IEEE Trans. Geosci. Remote Sens.*, Vol. 46, No. 8, 2224–2232, 2008.
16. D'Aria, D., A. M. Guarnieri, and F. Rocca, "Focusing bistatic synthetic aperture radar using dip move out," *IEEE Trans. Geosci. Remote Sens.*, Vol. 42, No. 7, 1362–1376, 2004.
17. Sun, J., S. Mao, W. Hong, and G. Wang, "Extended exact transfer function algorithm for bistatic SAR of translational invariant case," *Progress In Electromagnetics Research*, PIER 99, 89–108, 2009.
18. Wong, F. H. and T. S. Yeo, "New applications of nonlinear chirp scaling in SAR data processing," *IEEE Trans. Geosci. Remote Sens.*, Vol. 39, No. 5, 946–953, 2001.
19. Neo, Y., F. Wong, and I. G. Cumming, "A two-dimensional spectrum for bistatic SAR processing using series reversion," *IEEE Trans. Geosci. Remote Sens. Lett.*, Vol. 4, No. 2, 307–311, 2007.
20. Bamler, R., F. Meyer, and W. Liebhart, "Processing of bistatic SAR data from quasi-stationary configurations," *IEEE Trans. Geosci. Remote Sens.*, Vol. 45, No. 11, 3350–3358, 2007.
21. Carrara, W. G., R. S. Goodman, and R. M. Majewaki, *Spotlight Synthetic Aperture Radar: Signal Processing Algorithms*, Artech House, Norwood, MA, 1995.
22. Jakowatz, C. V., D. E. Wahl, D. C. Ghiglia, and P. A. Thompson, *Spotlight-mode Synthetic Aperture Radar: A Signal Processing Approach*, Kluwer Academic Publishers, 1996.
23. Rigling, B. D. and R. L. Moses, "Polar format algorithm for bistatic SAR," *IEEE Transactions on Aerospace and Electronic Systems*, Vol. 40, No. 4, 1147–1159, 2004.
24. Yuan, Y., J. Sun, and S. Mao, "PFA algorithm for airborne spotlight SAR imaging with nonideal motions," *IEE Proc., Radar*

Sonar Navig., Vol. 149, No. 4, 174–182, 2002.

25. Chan, Y. K. and V. C. Koo, "An introduction to synthetic aperture radar (SAR)," *Progress In Electromagnetics Research B*, Vol. 2, 27–60, 2008.
26. Chan, Y. K., V. C. Koo, B.-K. Chung, and H.-T. Chuah, "Modified algorithm for real time SAR signal processing," *Progress In Electromagnetics Research C*, Vol. 1, 159–168, 2008.
27. Lim, T. S., C.-S. Lim, V. C. Koo, H.-T. Ewe, and H.-T. Chuah, "Autofocus algorithms performance evaluations using an integrated SAR product simulator and processor," *Progress In Electromagnetics Research B*, Vol. 3, 315–329, 2008.
28. Lim, T. S., V. C. Koo, H.-T. Ewe, and H.-T. Chuah, "A SAR autofocus algorithm based on particle swarm optimization," *Progress In Electromagnetics Research B*, Vol. 1, 159–176, 2008.
29. Chan, Y. K. and S. Y. Lim, "Synthetic aperture radar (SAR) signal generation," *Progress In Electromagnetics Research B*, Vol. 1, 269–290, 2008.
30. Cumming, I. G. and F. Wong, *Digital Processing of Synthetic Aperture Radar*, Artech House, Norwood, MA, 2005.